Journal of Computational Physics 228 (2009) 8034–8052

Contents lists available at ScienceDirect

Journal of Computational Physics

journal homepage: www.elsevier.com/locate/jcp

A dispersion-relation-preserving algorithm for a nonlinear shallow-water wave equation

P.H. Chiu [a], Long Lee [b,*], Tony W.H. Sheu [a,c]

[a] Department of Engineering Science and Ocean Engineering, National Taiwan University, Taipei, Taiwan, ROC
[b] Department of Mathematics, University of Wyoming, Laramie, Wyoming, USA
[c] Taida Institute of Mathematical Science (TIMS), National Taiwan University, Taipei, Taiwan, ROC

ARTICLE INFO

Article history:
Received 28 March 2009
Received in revised form 22 July 2009
Accepted 27 July 2009
Available online 3 August 2009

Keywords:
Dispersion-relation-preserving
Nonlinear shallow-water wave equation
Implicit midpoint
Sixth-order
Helmholtz equation

ABSTRACT

The paper presents an iterative algorithm for studying a nonlinear shallow-water wave equation. The equation is written as an evolution equation, involving only first-order spatial derivatives, coupled with the Helmholtz equation. We propose a two-step iterative method that first solves the evolution equation by the implicit midpoint rule and then solves the Helmholtz equation using a three-point sixth-order compact scheme. The first-order derivative terms in the first step are approximated by a sixth-order dispersion-relation-preserving scheme that preserves the physically inherent dispersive nature. The compact Helmholtz solver, on the other hand, allows us to use relatively few nodal points in a stencil, while achieving a higher-order accuracy. The midpoint rule is a symplectic time integrator for Hamiltonian systems, which may be a preferable method to solve the spatially discretized evolution equation. To give an assessment of the dispersion-preserving scheme, we provide a detailed analysis of the dispersive and dissipative errors of this algorithm. Via a variety of examples, we illustrate the efficiency and accuracy of the proposed scheme by examining the errors in different norms and providing the rates of convergence of the method. In addition, we provide several examples to demonstrate that the conserved quantities of the equation are well preserved by the implicit midpoint time integrator. Finally, we compare the accuracy, elapsed computing time, and spatial and temporal rates of convergence among the proposed method, a complete integrable particle method, and the local discontinuous Galerkin method.

1. Introduction

The shallow-water wave equation (which has come to be known as the CH equation, for Camassa–Holm equation) [3],

$$u_t + 2\kappa u_x - u_{xxt} + 3uu_x = 2u_x u_{xx} + uu_{xxx}, \tag{1.1}$$

results from an asymptotic expansion of the Euler equations governing the motion of an inviscid fluid whose free surface can exhibit gravity-driven wave motion [4,18]. The small parameters used to carry out the expansion are the aspect ratio, whereby the depth of the fluid is assumed to be much smaller than the typical wavelength of the motion, and the amplitude ratio, or ratio between a typical amplitude of wave motion and the average depth of the fluid. Thus, the equation is a member of the class of weakly nonlinear (due to the smallness assumption on the amplitude parameter) and weakly dispersive (due to the long wave assumption parameter) models for water wave propagation. However, at variance with its celebrated close

* Corresponding author. Tel.: +1 307 766 4368; fax: +1 307 766 6838.
E-mail address: llee@uwyo.edu (L. Lee).

0021-9991/$ - see front matter © 2009 Elsevier Inc. All rights reserved.
doi:10.1016/j.jcp.2009.07.030

relatives in this class, such as the Korteweg-de Vries (KdV) and Benjamin–Bona–Mahony (BBM) equations, these small parameters are assumed to be linked only by a relative ordering, rather than by a power-law relation. This allows us to retain terms on the right-hand-side that would be of higher order with respect to both the KdV and BBM expansions, and, in principle, to consider dynamical regimes in which nonlinearity is somewhat dominant with respect to wave dispersion. This equation possesses the remarkable property of complete integrability, as evidenced by its Lax-pair representation, and permits an infinite number of nonlocal conserved properties [3,21]. When $\kappa = 0$ in Eq. (1.1), the equation becomes the dispersionless version of a shallow-water wave equation that admits peakon solutions.

There is extensive literature on numerical analysis and implementation for the KdV type of equations; however, numerical algorithms for the shallow-water wave equation have only received attention recently. While no attempt will be made here to provide a detailed reference list, the following are examples of recent algorithms developed for the shallow-water wave equation. In [5–9], a completely integrable particle method is introduced that solves the equation in infinite domains, semi-infinite domains with the zero boundary condition on one side, periodic domains, and homogeneous finite domains. The particle method is based on the Hamiltonian structure of the equation, an algorithm corresponding to a completely integrable particle lattice. Each periodic particle in this method travels along a characteristic curve of the shallow-water wave model, determined by solving a system of nonlinear integro-differential equations. This system of nonlinear integro-differential equations can be viewed as particle interaction through a long-range potential (here position and momentum dependent). Besides the particle method, a method based on multipeakons is developed in [16] for Eq. (1.1). The convergence proof of this method is given in [17]. A finite difference scheme that can handle general H^1 initial data is introduced in [13]. A pseudospectral method is developed in [19] for the travelling wave solution of Eq. (1.1). Similar methods, a semi-discretization Fourier–Galerkin method and a Fourier-collocation method, are developed in [20]. A finite volume method, within the adaptive upwinding context, is developed for the peakon solution of Eq. (1.1) [1]. A local discontinuous Galerkin finite element method is developed in [24].

Eq. (1.1) involves two third-order derivative terms, uu_{xxx} and u_{xxt}. For most numerical schemes, except the particle method and the related methods, certain care is required to discretize those terms in order to achieve a higher-order accuracy while preserving the physically inherent dispersive nature of the equation. In the study, however, we avoid discretizing both of the third-order derivative terms by applying the Helmholtz operator to u

$$m(x,t) \equiv (1 - \partial_x^2)\, u(x,t), \tag{1.2}$$

and rewrite the Eq. (1.1) into an equivalent formulation

$$m_t = -2(m + \kappa)\, u_x - u m_x. \tag{1.3}$$

Note that Eq. (1.3) involves only the first-order derivative terms. As a result of the new formulation, we develop a two-step iterative numerical algorithm that first solves the evolution Eq. (1.3) by a midpoint time integrator and then solves the Helmholtz equation (1.2) with a three-point sixth-order compact scheme. The first-order derivative terms in the first step are approximated by a sixth-order dispersion-relation-preserving scheme that preserves the physically inherent dispersive nature. The compact Helmholtz solver, on the other hand, allows us to use relatively few nodal points in a stencil, while achieving a higher-order accuracy. The principle of the two-step iterative algorithm is to solve the first-order equation and then to solve the Helmholtz equation, repeating the process until the convergence criterions are satisfied.

It is worth noting that the two-step iterative algorithm developed in the following sections can be generalized into a framework of numerical methods that solve a whole class of partial differential equations involving the Helmholtz operator [10]. We also note that a higher-dimensional extension of the shallow-water wave equation is the very well-known Navier–Stokes-alpha turbulence model [11]. The proposed one-dimensional algorithm can be directly extended to solve the higher-dimensional model (extension for other methods, such as the integrable particle method, may not be so straightforward). The Navier–Stokes-alpha model potentially could answer some long-standing questions in the field of turbulent flows, and an accurate numerical method could be the key to achieving the goal. A careful examination of the one-dimensional algorithm is a fundamental first step on the path towards the development of a higher-dimensional algorithm.

2. Two-step iterative algorithm

The evolution Eq. (1.3) can be solved by a standard method of lines (MOL). Let $m^n = m(t^n, x)$ and $m^{n+1} = m(t^n + \Delta t, x)$ be the semi-discretized m values at time level$n$ and $n+1$, respectively. The MOL, using the midpoint time integrator, for Eq. (1.3) yields

$$\frac{m^{n+1} - m^n}{\Delta t} = -2(m^{n+1/2} + \kappa)\, u_x^{n+1/2} - u^{n+1/2}\, m_x^{n+1/2}, \tag{2.1}$$

where

$$m^{n+1/2} = \frac{1}{2}(m^{n+1} + m^n) \quad \text{and} \quad u^{n+1/2} = \frac{1}{2}(u^{n+1} + u^n). \tag{2.2}$$

The first-order derivative terms $m_x^{n+1/2}$ and $u_x^{n+1/2}$ are approximated by a sixth-order dispersion-relation-preserving scheme, using the nodal values of (2.2). We discuss the sixth-order scheme in detail in the next section. It is worth noting that the

midpoint time integrator is a symplectic integrator for Hamiltonian systems [2,15], which may be a preferable method for solving the system of spatially discretized equations. Since the evolution Eq. (2.1) is coupled with the Helmholtz equation, it is necessary to introduce an iterative scheme to obtain m^{n+1} and u^{n+1} from m^n and u^n. We do this by alternating between solving Eq. (2.1) and the Helmholtz equation, as described in the following steps:

- *Step 1*: Given an initial guess for $u^{n+1/2}$ and $m^{n+1/2}$, denoted $u^{(0),n+1/2}$ and $m^{(0),n+1/2}$ respectively, we solve the evolution Eq. (2.1) to obtain $m^{(1),n+1}$. The initial guess is based on Taylor series expansions:

$$\begin{aligned} m^{(0),n+1/2} &= 1.5m^n - 0.5m^{n-1}, \\ u^{(0),n+1/2} &= 1.5u^n - 0.5u^{n-1}, \end{aligned} \tag{2.3}$$

  where $n \geqslant 1$. When $n = 0$, we impose $m^{(0),1/2} = m_0$ and $u^{(0),1/2} = u_0$, where u_0 is the initial condition and $m_0 = u_0 - u_{0xx}$.
- *Step 2*: Using $m^{(1),n+1}$ and a three-point sixth-order compact scheme, we solve the Helmholtz equation to obtain $u^{(1),n+1}$.
- *Step 3*: Find $m^{(1),n+1/2}$ and $u^{(1),n+1/2}$ by Eq. (2.2) and solve the evolution Eq. (2.1) to obtain $m^{(2),n+1}$.
- *Step 4*: Repeat *Step 2* and *Step 3* for the next iteration until the $(i+1)^{th}$ iteration, for which the residuals, in the maximum norm, of both Eq. (2.1) and the Helmholtz equation are less than our convergence criterions:

$$\begin{aligned} &\max_{x_j, j=1,N} \left| \frac{m^{(i+1),n+1} - m^n}{\Delta t} + (2(m^{n+1/2} + \kappa)u_x^{n+1/2} + u^{n+1/2} m_x^{n+1/2}) \right| \leqslant \varepsilon, \\ &\max_{x_j, j=1,N} |m^{(i+1),n+1} - (u^{(i+1),n+1} - u_{xx}^{(i+1),n+1})| \leqslant \varepsilon, \end{aligned} \tag{2.4}$$

where N is the number of grid points, and the value for the threshold error ε is typically chosen to be 10^{-12} throughout our computations. Our numerical experiments indicate that the number of iterations needed for convergence with this value is less than 20 in general.

We remark that for the initial guess (2.3), if we let $t^{n+1/2} = t^n + \Delta t/2$, the Taylor series expansions for $m(t^n)$ and $m(t^{n-1})$ about $t^{n+1/2}$ give rise to

$$m(t^{n+1/2}) = 1.5m(t^n) - 0.5m(t^{n-1}) + O(\Delta t^2). \tag{2.5}$$

Therefore, if we let $m^n = m(t^n)$ and $m^{n-1} = m(t^{n-1})$, the initial guess $m^{n+1/2}$ in (2.3) is an $O(\Delta t^2)$ approximation for $m(t^{n+1/2})$.

3. Dispersion-relation-preserving scheme

The spacial accuracy of the proposed scheme depends on how accurately we can approximate the first-order derivative terms. In particular, if the equation of interest is a dispersive equation, such as the shallow-water wave equation, a dispersion-relation-preserving scheme is necessary to ensure the accuracy of numerical solutions. In this section, we develop a dispersion-relation-preserving scheme for the first-order derivative terms.

Suppose that the first derivative term at the grid point i is approximated by the following algebraic equation:

$$\left.\frac{\partial m}{\partial x}\right|_i = \frac{1}{h}(c_1 m_{i-5} + c_2 m_{i-4} + c_3 m_{i-3} + c_4 m_{i-2} + c_5 m_{i-1} + c_6 m_i + c_7 m_{i+1} + c_8 m_{i+2} + c_9 m_{i+3}). \tag{3.1}$$

For simplicity, we consider the case involving only the positive convective coefficient in the above equation, since the derivation will be the same for the negative convective coefficient.

Derivation of expressions for $c_1 \sim c_9$ is followed by applying the Taylor series expansions for $m_{i\pm1}, m_{i\pm2}, m_{i\pm3}, m_{i-4}$ and m_{i-5} with respect to m_i and then eliminating the seven leading error terms derived in the modified equation. Elimination of these error terms enables us to derive the following set of algebraic equations:

$$c_1 + c_2 + c_3 + c_4 + c_5 + c_6 + c_7 + c_8 + c_9 = 0, \tag{3.2}$$

$$-5c_1 - 4c_2 - 3c_3 - 2c_4 - c_5 + c_7 + 2c_8 + 3c_9 = 1, \tag{3.3}$$

$$\frac{25}{2}c_1 + 8c_2 + \frac{9}{2}c_3 + 2c_4 + + \frac{1}{2}c_5 \frac{1}{2}c_7 + 2c_8 + \frac{9}{2}c_9 = 0, \tag{3.4}$$

$$-\frac{125}{6}c_1 - \frac{32}{3}c_2 - \frac{9}{2}c_3 - \frac{4}{3}c_4 - \frac{1}{6}c_5 + \frac{1}{6}c_7 + \frac{4}{3}c_8 + \frac{9}{2}c_9 = 0, \tag{3.5}$$

$$\frac{625}{24}c_1 + \frac{32}{3}c_2 + \frac{27}{8}c_3 + \frac{2}{3}c_4 + \frac{1}{24}c_5 + \frac{1}{24}c_7 + \frac{2}{3}c_8 + \frac{27}{8}c_9 = 0, \tag{3.6}$$

$$-\frac{625}{24}c_1 - \frac{128}{15}c_2 - \frac{81}{40}c_3 - \frac{4}{15}c_4 - \frac{1}{120}c_5 + \frac{1}{120}c_7 + \frac{4}{15}c_8 + \frac{81}{40}c_9 = 0, \tag{3.7}$$

$$\frac{3125}{144}c_1 + \frac{256}{45}c_2 + \frac{81}{80}c_3 + \frac{4}{45}c_4 + \frac{1}{720}c_5 + \frac{1}{720}c_7 + \frac{4}{45}c_8 + \frac{81}{80}c_9 = 0 \tag{3.8}$$

To uniquely determine all nine introduced coefficients shown in (3.1), we need two more equations. Following the suggestion in [22], we derive the equations by preserving the dispersion relation that governs the relation between the angular

frequency and the wavenumber of the first-order dispersive term. To obtain the two extra equations based on the principle of preservation of the dispersion relation, we note that the Fourier transform pair for m is

$$\tilde{m}(k) = \frac{1}{2\pi} \int_{-\infty}^{+\infty} m(x)\ e^{-\mathbf{i}kx}\ dx, \tag{3.9}$$

$$m(x) = \int_{-\infty}^{+\infty} \tilde{m}(\alpha)\ e^{\mathbf{i}kx}\ dk. \tag{3.10}$$

If we perform the Fourier transform on each term shown in Eq. (3.1), we obtain that the wavenumber k is approximated by the following expression

$$k \simeq \frac{-\mathbf{i}}{h}(c_1\ e^{-\mathbf{i}5kh} + c_2\ e^{-\mathbf{i}4kh} + c_3\ e^{-\mathbf{i}3kh} + c_4\ e^{-\mathbf{i}2kh} + c_5\ e^{-\mathbf{i}kh} + c_6 + c_7\ e^{\mathbf{i}kh} + c_8\ e^{\mathbf{i}2kh} + c_9\ e^{\mathbf{i}3kh}), \tag{3.11}$$

where $\mathbf{i} = \sqrt{-1}$.

Supposing that the effective wavenumber $\tilde{k}$ is exactly equal to the right-hand side of Eq. (3.11) [22], we have $k \approx \tilde{k}$. In order to acquire a better dispersive accuracy, $\tilde{k}$ should be made as close to k as possible. This implies that E defined in the sense of the 2-norm of the error between k and $\tilde{k}$ will be the local minimum for such a $\tilde{k}$. The error E is defined as follows

$$E(k) = \int_{-\frac{\pi}{2}}^{\frac{\pi}{2}} |kh - \tilde{k}h|^2\ d(kh) = \int_{-\frac{\pi}{2}}^{\frac{\pi}{2}} |\gamma - \tilde{\gamma}|^2\ d\gamma, \tag{3.12}$$

where h is denoted as the grid size and $\gamma = kh$. For E to be a local minimum, we assume the following two extreme conditions

$$\frac{\partial E}{\partial c_4} = 0, \tag{3.13}$$

$$\frac{\partial E}{\partial c_5} = 0. \tag{3.14}$$

Under the above prescribed extreme conditions, the two algebraic equations needed for the coefficients to be uniquely determined are

$$-\frac{4}{3}c_1 + 4c_3 + 2\pi c_4 + 4c_5 - \frac{4}{3}c_7 + \frac{4}{5}c_9 + \pi = 0, \tag{3.15}$$

$$-\frac{4}{3}c_2 + 4c_4 + 2\pi c_5 + 4c_6 - \frac{4}{3}c_8 + 4 = 0. \tag{3.16}$$

We remark that for a truly dispersion-relation-preserving scheme, i.e. the error E is truly a local minimum on the parameter space, one will need to impose $\partial E/\partial c_i = 0$ for $i = 1, \ldots, 9$ to obtain nine equations for the coefficients. Our approach, instead, (i) ensures the higher-order accuracy by letting the coefficients satisfy the Taylor series expansions and (ii) partially enforces the requirements for a dispersion-relation-preserving scheme. Our numerical experiments show that the upwinding scheme for the first-order derivative obtained by taking the derivatives about c_4 and c_5 for E (Eqs. (3.13) and (3.14)) produces the least numerical errors. It is also worth noting that the integration interval shown in Eq. (3.12) needs to be sufficiently wide to cover a complete period of sine (or cosine) waves.

Eqs. (3.15) and (3.16) together with Eqs. (3.2)–(3.8) yield the coefficients:

$$c_1 = \frac{1}{50}\left(\frac{1575\pi^2 - 8340\pi + 10624}{-12432\pi + 17408 + 2205\pi^2}\right), \tag{3.17}$$

$$c_2 = -\frac{3}{100}\left(\frac{7875\pi^2 - 42480\pi + 55552}{-12432\pi + 17408 + 2205\pi^2}\right), \tag{3.18}$$

$$c_3 = \frac{1}{75}\left(\frac{55125\pi^2 - 303240\pi + 406976}{-12432\pi + 17408 + 2205\pi^2}\right), \tag{3.19}$$

$$c_4 = -\frac{1}{10}\left(\frac{-62160\pi + 85888 + 11025\pi^2}{-12432\pi + 17408 + 2205\pi^2}\right), \tag{3.20}$$

$$c_5 = -\frac{12}{5(21\pi - 64)}, \tag{3.21}$$

$$c_6 = -\frac{7}{100}\left(\frac{17325\pi^2 - 103440\pi + 153344}{-12432\pi + 17408 + 2205\pi^2}\right), \tag{3.22}$$

$$c_7 = \frac{1}{25}\left(\frac{55125\pi^2 - 318360\pi + 457664}{-12432\pi + 17408 + 2205\pi^2}\right), \tag{3.23}$$

$$c_8 = -\frac{9}{50}\left(\frac{2625\pi^2 - 15440\pi + 22656}{-12432\pi + 17408 + 2205\pi^2}\right), \tag{3.24}$$

$$c_9 = \frac{1}{6}\left(\frac{15\pi - 44}{105\pi - 272}\right). \tag{3.25}$$

It is easy to show that the proposed upwinding scheme for the first-order derivative is sixth-order spatially accurate:

$$\frac{\partial m}{\partial x} = \frac{\partial m}{\partial x}|_{exact} - \frac{48}{175}\left(\frac{105\pi - 332}{-12432\pi + 17408 + 2205\pi^2}\right)h^6\frac{\partial^7 m}{\partial x^7} + \left(\frac{7875\pi^2 - 39360\pi + 45824}{-12432\pi + 17408 + 2205\pi^2}\right)h^7\frac{\partial^8 m}{\partial x^8} + O(h^8) + \cdots. \tag{3.26}$$

4. Three-point sixth-order accurate compact Helmholtz solver

We introduce a compact scheme for solving the Helmholtz equation in this section. It is well known that in order to obtain a higher-order numerical method for the Helmholtz equation, one can always introduce more points in a stencil. The improved accuracy, however, comes at the cost of an expensive matrix calculation, due to the wider stencil. With the aim of developing a numerical scheme that is higher-order accurate while using relative few stencil points in the finite difference discretization, we introduce a compact scheme involving only three points in a stencil, but is sixth-order accurate.

Consider the following prototype equation

$$\frac{\partial^2 u}{\partial x^2} - ku = f(x). \tag{4.1}$$

We first denote the values of $\partial^2 u/\partial x^2$, $\partial^4 u/\partial x^4$ and $\partial^6 u/\partial x^6$ at a nodal point i as

$$\left.\frac{\partial^2 u}{\partial x^2}\right|_i = s_i, \tag{4.2}$$

$$\left.\frac{\partial^4 u}{\partial x^4}\right|_i = v_i, \tag{4.3}$$

$$\left.\frac{\partial^6 u}{\partial x^6}\right|_i = w_i. \tag{4.4}$$

The compact scheme at point i starts with relating v, s and w with u as follows:

$$\delta_0 h^6 w_i + \gamma_0 h^4 v_i + \beta_0 h^2 s_i = \alpha_1 u_{i+1} + \alpha_0 u_i + \alpha_{-1} u_{i-1}. \tag{4.5}$$

Based on physics, it is legitimate to set $\alpha_1 = \alpha_{-1}$ since the Helmholtz equation is elliptic in nature. Having set $\alpha_1 = \alpha_{-1}$, the derivation is followed by expanding $u_{i\pm1}$ with respect to u_i. Substitution of these Taylor-series expansion equations into Eq. (4.5) leads to

$$\delta_0 h^6 w_i + \gamma_0 h^4 v_i + \beta_0 h^2 s_i = (\alpha_0 + 2\alpha_1)u_i + \frac{h^2}{2!}(2\alpha_1)\frac{\partial^2 u_i}{\partial x^2} + \frac{h^4}{4!}(2\alpha_1)\frac{\partial^4 u_i}{\partial x^4} + \frac{h^6}{6!}(2\alpha_1)\frac{\partial^6 u_i}{\partial x^6} + \frac{h^8}{8!}(2\alpha_1)\frac{\partial^8 u_i}{\partial x^8} + \cdots. \tag{4.6}$$

Through a term-by-term comparison of the derivatives shown in Eq. (4.6), five simultaneous algebraic equations can be derived. Hence, the introduced free parameters can be determined as $\alpha_1 = \alpha_{-1} = -1, \alpha_0 = 2, \beta_0 = -1, \gamma_0 = -\frac{1}{12}$ and $\delta_0 = -\frac{1}{360}$. Note that $w_i = k^3 u_i + k^2 f_i + k\frac{\partial^2 f_i}{\partial x^2} + \frac{\partial^4 f_i}{\partial x^4}$, $v_i = k^2 u_i + k f_i + \frac{\partial^2 f_i}{\partial x^2}$, and $s_i = k u_i + f_i$. Eq. (4.5) can then be expressed as

$$\alpha_1 u_{i+1} + (\alpha_0 - \beta_0 h^2 k - \gamma_0 h^4 k^2 - \delta_0 h^6 k^3)u_i + \alpha_1 u_{i-1} = \left[h^2\beta_0 f_i + h^4\gamma_0\left(k f_i + \frac{\partial^2 f_i}{\partial x^2}\right) + h^6\delta_0\left(k^2 f_i + k\frac{\partial^2 f_i}{\partial x^2} + \frac{\partial^4 f_i}{\partial x^4}\right)\right]. \tag{4.7}$$

It follows that

$$u_{i+1} - \left(2 + h^2 k + \frac{1}{12}h^4 k^2 + \frac{1}{360}h^6 k^3\right)u_i + u_{i-1} = h^2 f_i + \frac{1}{12}h^4\left(k f_i + \frac{\partial^2 f_i}{\partial x^2}\right) + \frac{1}{360}h^6\left(k^2 f_i + k\frac{\partial^2 f_i}{\partial x^2} + \frac{\partial^4 f_i}{\partial x^4}\right). \tag{4.8}$$

Using the proposed scheme, the corresponding modified equation for (4.1) can be derived as follows, after performing some algebraic manipulation:

$$\frac{\partial^2 u}{\partial x^2} - k u = f + \frac{h^6}{20160}\frac{\partial^8 u}{\partial x^8} + \frac{h^8}{1814400}\frac{\partial^{10} u}{\partial x^{10}} + \cdots + H.O.T. \tag{4.9}$$

Eq. (4.9) shows that the 3-point stencil scheme is indeed sixth-order accurate. We implement a multigrid method using the V-cycle and fully-weighted projection/prolongation with the red-black Gauss-Seidel smoother to solve the system of algebraic equations arising from discretization of the proposed scheme.

5. Error analysis

In this section, we assess the proposed two-step iterative algorithm by providing a detailed error analysis for the midpoint time integrator and the dispersion-relation-preserving scheme. After this we show the von Neumann analysis for the midpoint time integrator. Close observation reveals that Eq. (2.1) is essentially a discretized version of a one-dimensional linear scalar convection-reaction equation. Hence to analyze the error due to the proposed time-stepping algorithm and the dispersion-relation-preserving scheme in the first step of the two-step iterative algorithm, we simply analyze numerical solutions of a linear scalar convection-reaction equation obtained by the proposed schemes.

Consider a one-dimensional linear scalar convection-reaction equation

$$\frac{\partial \phi}{\partial t} + c_a \frac{\partial \phi}{\partial x} + c_r \phi = 0, \tag{5.1}$$

where c_a and c_r are given constants. Applying the midpoint time integrator to the equation yields

$$\frac{\phi^{n+1} - \phi^n}{\Delta t} + \frac{1}{2}[c_a\ (\phi_x^{n+1} + \phi_x^n) + c_r\ (\phi^{n+1} + \phi^n)] = 0. \tag{5.2}$$

Substituting ϕ_x^{n+1} and ϕ_x^n, approximated by the proposed sixth-order dispersion-relation-preserving scheme (3.17)–(3.23), (3.23) and (3.25), into the above equation results in a nine-point-stencil difference equation at an interior point i:

$$\begin{aligned}
&\phi_i^{n+1} + \frac{1}{2}(A_1\phi_{i-5}^{n+1} + A_2\phi_{i-4}^{n+1} + A_3\phi_{i-3}^{n+1} + A_4\phi_{i-2}^{n+1} + A_5\phi_{i-1}^{n+1} + A_6\phi_i^{n+1} + A_7\phi_{i+1}^{n+1} + A_8\phi_{i+2}^{n+1} + A_9\phi_{i+3}^{n+1}) \\
&\quad = \phi_i^n - \frac{1}{2}(A_1\phi_{i-5}^n + A_2\phi_{i-4}^n + A_3\phi_{i-3}^n + A_4\phi_{i-2}^n + A_5\phi_{i-1}^n + A_6\phi_i^n + A_7\phi_{i+1}^n + A_8\phi_{i+2}^n + A_9\phi_{i+3}^n),
\end{aligned} \tag{5.3}$$

where $A_i = c_a c_i \Delta t/h, i = 1, \ldots, 5$ and $7, 8, 9$, and $A_6 = c_a c_6 \Delta t/h + c_r \Delta t$. If the initial condition is $\phi(x, 0) = \exp(\ \mathbf{i} kx\ )$, then the exact solution of Eq. (5.1) is given by

$$\phi(x, t) = \exp\{\ -c_r t\ \} \exp\{\ \mathbf{i} k(x - c_a t)\}. \tag{5.4}$$

Suppose that a numerical solution is contaminated by numerical amplitude and phase errors and is expressed by

$$\tilde{\phi}(x, t) = \exp\left\{-\left(c_r \frac{k_r}{\gamma^2}\right)t\right\} \exp\left\{\mathbf{i} k\left(x - c_a \frac{k_i}{\gamma} t\right)\right\}, \tag{5.5}$$

where the wavenumber k and the so-called modified wavenumber $\gamma = kh$ are defined in Section 3, Eq. (3.11). It is clear that if $k_i = \gamma$ and $k_r = \gamma^2$, then we do not have either phase or amplitude errors. Since the errors propagate in both time and space, the propagated numerical solution can be written as

$$\tilde{\phi}(x + h, t + \Delta t) = \tilde{\phi}(x, t) \exp\left\{-\left(c_r \frac{k_r}{\gamma^2}\right)\Delta t\right\} \exp\left\{\mathbf{i} k\left(h - c_a \frac{k_i}{\gamma} \Delta t\right)\right\}, \tag{5.6}$$

or

$$\tilde{\phi}(x + h, t + \Delta t) = \tilde{\phi}(x, t) \exp(\mathbf{i} kh) \exp(\bar{p} + \mathbf{i}\bar{q}). \tag{5.7}$$

Comparing Eqs. (5.6) and (5.7), we obtain the amplitude and phase errors, in terms of k_r and k_i,

$$k_r = \frac{-\bar{p}}{\left(\frac{v_x R_x}{\gamma^2}\right)}, \tag{5.8}$$

$$k_i = \frac{-\bar{q}}{v_x}, \tag{5.9}$$

where

$$v_x = \frac{c_a \Delta t}{h}, \quad R_x = \frac{c_r h}{c_a}. \tag{5.10}$$

To determine $\bar{p}$ and $\bar{q}$ in Eqs. (5.8) and (5.9), letting $\phi_i^n = \tilde{\phi}(x, t)$ and substituting the expressions of $\phi_i, \phi_{i-1}, \phi_{i\pm2}, \phi_{i\pm3}, \phi_{i-4}$, and ϕ_{i-5} at the corresponding time levels, n or $n + 1$, into Eq. (5.3), we obtain

$$\begin{aligned}
&e^{\bar{p}}(e^{\mathbf{i}\bar{q}} + \frac{1}{2}(A_1 e^{\mathbf{i}(\bar{q}-5\gamma)} + A_2 e^{\mathbf{i}(\bar{q}-4\gamma)} + A_3 e^{\mathbf{i}(\bar{q}-3\gamma)} + A_4 e^{\mathbf{i}(\bar{q}-2\gamma)} + A_5 e^{\mathbf{i}(\bar{q}-\gamma)} + A_6 e^{\mathbf{i}\bar{q}} + A_7 e^{\mathbf{i}(\bar{q}+\gamma)} + A_8 e^{\mathbf{i}(\bar{q}+2\gamma)} + A_9 e^{\mathbf{i}(\bar{q}+3\gamma)})) \\
&\quad = 1 - \frac{1}{2}(A_1 e^{\mathbf{i}(-5\gamma)} + A_2 e^{\mathbf{i}(-4\gamma)} + A_3 e^{\mathbf{i}(-3\gamma)} + A_4 e^{\mathbf{i}(-2\gamma)} + A_5 e^{\mathbf{i}(-\gamma)} + A_6 + A_7 e^{\mathbf{i}(\gamma)} + A_8 e^{\mathbf{i}(2\gamma)} + A_9 e^{\mathbf{i}(3\gamma)}).
\end{aligned} \tag{5.11}$$

From the imaginary and real parts of the above equation, we obtain $\bar{p}$ as functions of $\bar{q}$:

$$\textit{from the imaginary part of } (5.11): \bar{p} = \log\left\{\frac{\frac{1}{2}\bar{n}}{(1+\frac{1}{2}\bar{m})\sin\bar{q} - \frac{1}{2}\bar{n}\cos\bar{q}}\right\}, \tag{5.12}$$

$$\textit{from the real part of } (5.11): \bar{p} = \log\left\{\frac{1-\frac{1}{2}\bar{m}}{(1+\frac{1}{2}\bar{m})\cos\bar{q} + \frac{1}{2}\bar{n}\sin\bar{q}}\right\}, \tag{5.13}$$

where

$$\bar{m} = A_6 + (A_5 + A_7)\cos\gamma + (A_4 + A_8)\cos(2\gamma) + (A_3 + A_9)\cos(3\gamma) + A_2\cos(4\gamma) + A_1\cos(5\gamma), \tag{5.14}$$

$$\bar{n} = (A_5 - A_7)\sin\gamma + (A_4 - A_8)\sin(2\gamma) + (A_3 - A_9)\sin(3\gamma) + A_2\sin(4\gamma) + A_1\sin(5\gamma), \tag{5.15}$$

and log is the natural logarithm.

Solving Eqs. (5.12) and (5.13) for $\bar{q}$, we obtain

$$\bar{q} = -\tan^{-1}\left(\frac{4\bar{n}}{\bar{n}^2 - 4 + \bar{m}^2}\right). \tag{5.16}$$

It is shown in Fig. 5.1(a) that k_i and γ are visually indistinguishable when $\gamma \leqslant 1.9$. This means that there are small or no errors for the method when $\gamma \leqslant 1.9$. Here k_i is plotted against γ for $\nu_x = 0.1$ and $R_x = 1$. For a large γ, either due to a large step size h or due to a larger wavenumber k, or both, the predicted phase of the numerical solution is less accurate. Similarly for the amplitude error, Fig. 5.1(b) shows that k_r and γ^2 are visually indistinguishable when $\gamma \leqslant 1.7$.

In addition to phase and amplitude errors, the numerical group velocity is also an indication of the quality of numerical algorithms, especially for numerical algorithms that solve dispersive equations. From Eq. (5.5), the numerical group velocity is found by

$$C_g = \frac{d\omega}{dk}, \quad \text{where} \quad \omega = c_a k \frac{k_i}{\gamma}. \tag{5.17}$$

When $k_i = \gamma$, the exact group velocity $C_e = c_a$. Fig. 5.2 plots the ratio of the numerical group velocity C_g and the exact group velocity C_e versus γ. It shows that when $\gamma \leqslant 1.7$, the numerical group velocity and the exact group velocity are almost identical. When γ increases, the numerical group velocity becomes less accurate.

The von Neumann analysis [23] shows that the proposed midpoint time integrator is unconditionally stable. To this end, define the amplification factor of the numerical solution at the grid point i to be

$$G = \frac{\phi_i^{n+1}}{\phi_i^n}, \tag{5.18}$$

and G can be written in the form

$$G = e^{\bar{p}}(\cos\bar{q} + \mathbf{i}\sin\bar{q}), \tag{5.19}$$

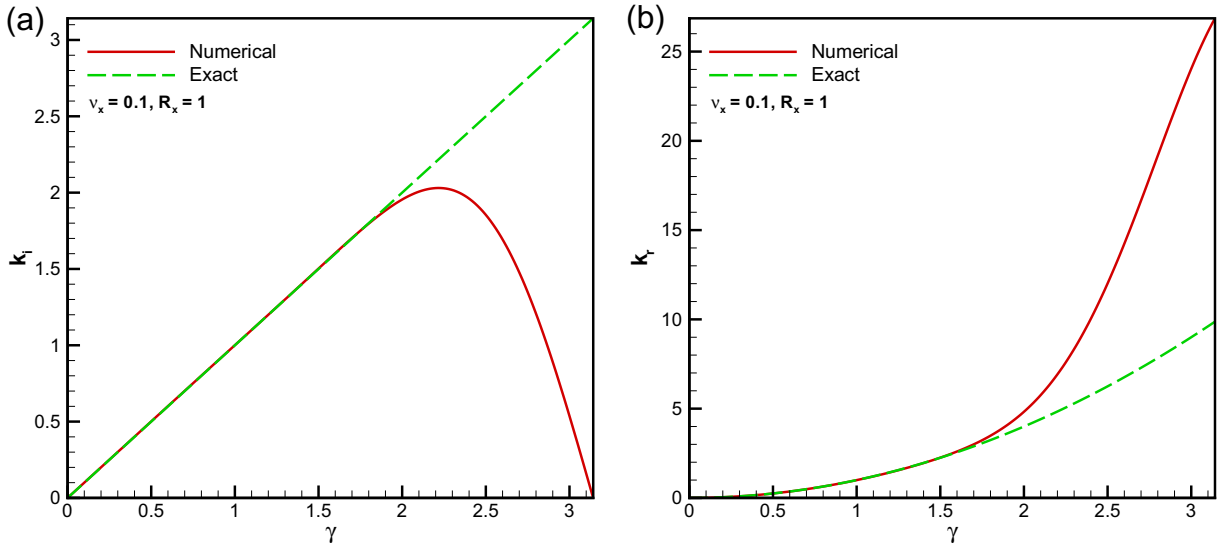

Fig. 5.1. The dissipation and phase (dispersion) error analysis. (a) The plot of k_i, the phase error plot. k_i and the modified wavenumber γ are visually indistinguishable when $\gamma \leqslant 1.9$. (b) The plot of k_r, the dissipation error plot. k_r and γ^2 are visually indistinguishable when $\gamma \leqslant 1.7$.

where $\bar{p}$ and $\bar{q}$ are the same as those defined in (5.7), (5.12), (5.13), and (5.16). Define the modified frequency

$$\chi_x = \frac{2\pi\bar{\bar{m}}}{2L}h, \quad \bar{\bar{m}} = 0, 1, 2, 3, \ldots, M, \tag{5.20}$$

where h is the grid size, and $2L$ is the period of fundamental frequency ($\bar{\bar{m}} = 1$). Since $Mh = L$, we have $0 \leqslant \chi_x <\leqslant \pi$. As shown in Fig. 5.3(a), since the magnitude of the modulus $|G|$, plotted versus χ_x, is smaller than one, by definition the proposed scheme is classified to be unconditionally stable. The amplification factor shown in (5.19) can be rewritten in the exponential form as $G = |G|\, e^{\mathbf{i}\,\theta}$, where the phase angle θ is defined to be

$$\theta = \tan^{-1}\left|\frac{\mathrm{Im}(G)}{\mathrm{Re}(G)}\right|. \tag{5.21}$$

The exact phase angle is $\theta_e = -\chi_x\, v_x$, where v_x is given in (5.10), and the relative phase-shift error is then given as

$$\mathscr{S} = \frac{\theta}{\theta_e} = \frac{\tan^{-1}\left|\frac{\mathrm{Im}(G)}{\mathrm{Re}(G)}\right|}{-\chi_x\, v_x}. \tag{5.22}$$

Fig. 5.3(b) shows $\mathscr{S}$ plotted versus χ_x for $v_x = 0.1$ and $R_x = 1$. It shows that $\mathscr{S} = 1$ before χ_x reaches $\pi/2$, *i. e.* the relative phase-shift error is either very small or nonexistent before the modified frequency χ_x reaches $\pi/2$.

6. Numerical results and validation

In this section, we provide several test problems to validate the proposed scheme and elucidate its computational properties.

6.1. Travelling wave solution in periodic domains

The first example is the traveling wave solution in periodic domains considered in [8,9]. The periodic travelling wave solution is given by $u(x,t) = U(x - c\,t)$, provided that the minima of u are located at $u = 0$ and the wave elevation is positive. In this case one finds that the solution of the travelling wave equation is given by

$$U' = \pm\sqrt{\frac{-U^3 + (c - 2\kappa)U^2 + C(A)\,U}{c - U}}, \tag{6.1}$$

where c and A are denoted as the wave speed and the wave amplitude, respectively, and the integration constant C is a function of A. Integration of Eq. (6.1) leads to the expression,

$$x = \frac{2}{\sqrt{b_1(b_2 - b_3)}}(b_1 - b_2)\Pi(\varphi, \beta^2, T). \tag{6.2}$$

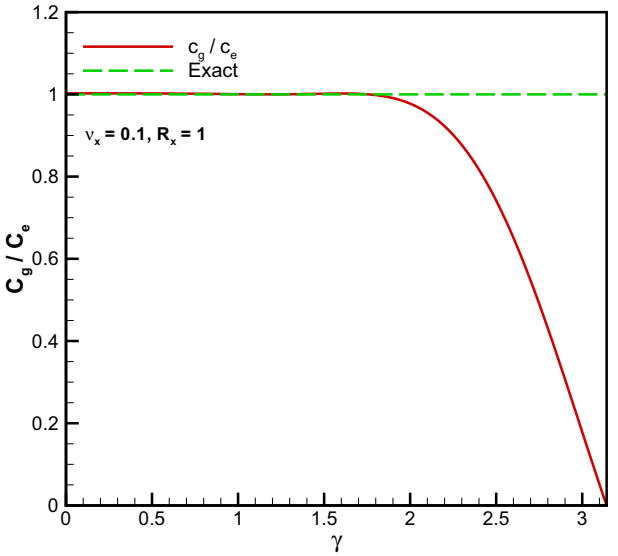

Fig. 5.2. Plots of the ratio of group velocity $\frac{c_g}{c_e}$ against the wavenumber γ at $R_x = 1$ and $v_x = 0.1$.

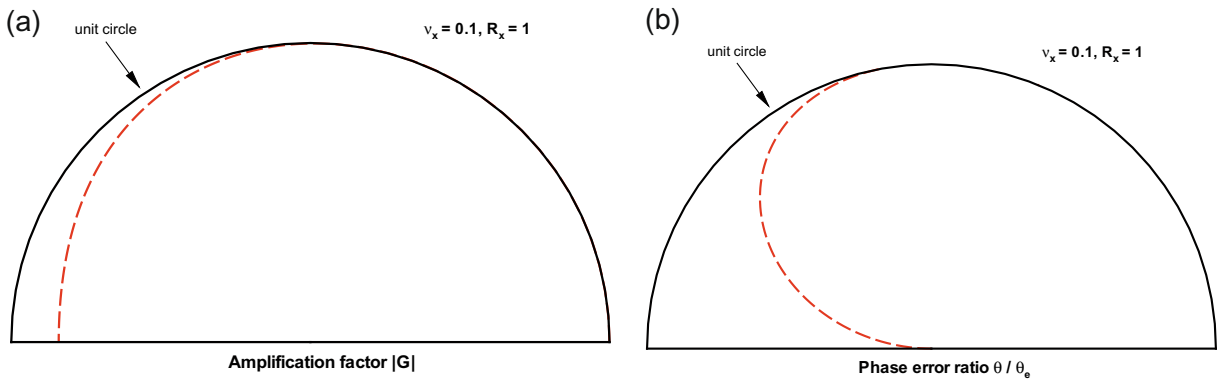

Fig. 5.3. Plots of $|G|$ and $\mathscr{S}$ versus χ_x at $v_x = 0.1$ and $R_x = 1$. Note that the angle χ_x is from 0 and π, counterclockwise. (a) The modulus of amplification factor $|G|$. (b) The relative phase-shift error $\mathscr{S}$. They show that both the amplitude and the phase either have very small errors or have no errors at all before the modified frequency χ_x reaches $\pi/2$.

The wavelength L of this periodic solution can be written as

$$L = \frac{4}{\sqrt{b_1(b_2 - b_3)}}(b_1 - b_2)\Pi(\varphi, \beta^2, T). \tag{6.3}$$

Details about the variables $x, \varphi, \beta, b_i\,(i = 1, \ldots, 3)$, c, and T are discussed in [8,9].

The parameters used in the test problem are $c = 2, \kappa = 1/2$, and the integration constant $C = 1$, which altogether yield the wavelength (period) of $L \approx 6.3019$ according to Eq. (6.3). The total time for the wave to travel through the domain and back to the initial position is $t = 3.1509$. The time step used in this calculation is $\Delta t = \frac{1}{4}\Delta x$ while the grid size is $\Delta x = 0.0492$ (or 128 cells). Fig. 6.1(a) shows the numerical and the exact solutions at $t = 0.788$. The initial data is the dashed line. A good agreement with the analytic solution is clearly demonstrated. To show that the proposed scheme is phase accurate, we also plot the predicted solution at $t = 3.1509$. As Fig. 6.1(b) is shown, the waveform over one period of time and the waveform of the initial data are visually identical.

It was shown in [5] that Eq. (1.1) can be written as

$$\frac{\partial W_x}{\partial t} + \frac{\partial (uW_x)}{\partial x} = 0, \tag{6.4}$$

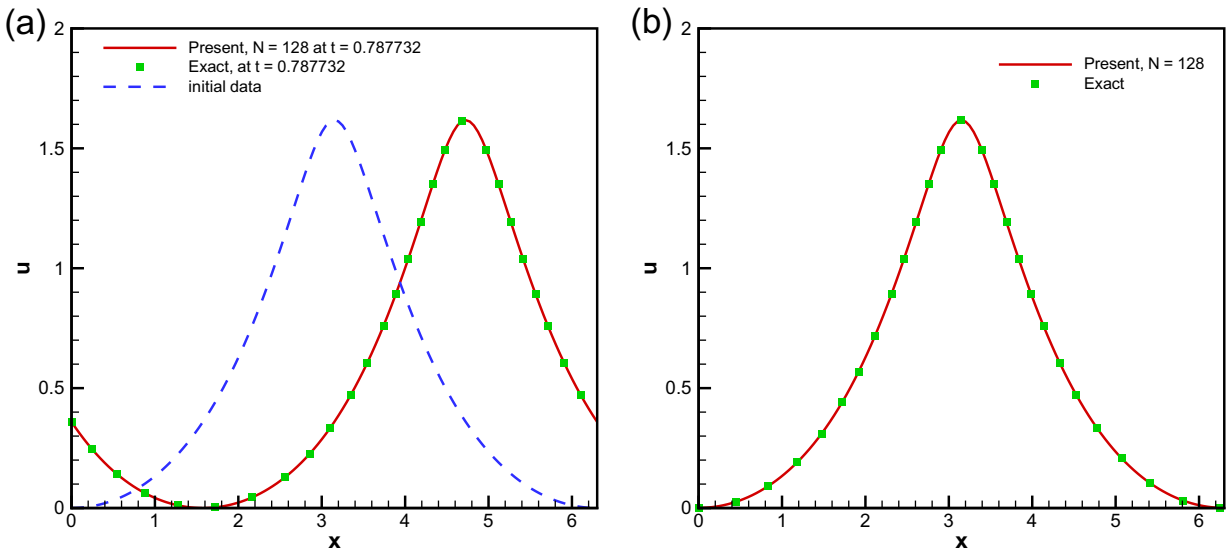

Fig. 6.1. The predicted traveling wave solution at (a) $t = 0.787732$, (b) $t = 3.1509$ (over one period). The numerical solutions are compared with the exact solutions that are plotted using square boxes in the illustrations.

where $W_x(\equiv \frac{\partial W}{\partial x})$ is defined as $\sqrt{m+\kappa}$, and $m = u - u_{xx}$. If we define

$$W = \int_0^L W_x \, dx, \tag{6.5}$$

then we can write Eq. (6.4) as

$$W_t + uW_x = 0. \tag{6.6}$$

This is an advection equation, where the conserved quantity W is advected by u and is therefore a constant in time. In Fig. 6.2, we plot the conserved quantities, mass, the Hamiltonians, and W versus time, where the mass and the Hamiltonians are defined as

$$M = \int_0^L u dx, \quad H_1 = \frac{1}{2}\int_0^L (u^2 + (u_x)^2) dx, \quad H_2 = \frac{1}{2}\int_0^L (u^3 + u(u_x)^2 + 2\kappa u^2) dx. \tag{6.7}$$

Fig. 6.2 clearly shows that the mass is well preserved, with the magnitude of 3.428, by the proposed algorithm. The Hamiltonians H_1 and H_2 are also invariant with the values of 2.996 and 5.163. The conserved quantity W is well preserved by the algorithm and has the value 5.452.

We conduct both grid and time refinement studies for the proposed method. The spatial rate of convergence test is carried out at the constant time step, $\Delta t = 0.12308 \times 10^{-3}$, that is much smaller than the grid size of the finest grid. As for the temporal rate of convergence test, we simply consider the case using a fixed grid size $\Delta x = 0.0492$, which is smaller in magnitude than the finest time step used in our calculation. The final time for both tests is $t = 3.1509$. The spatial and temporal rates of

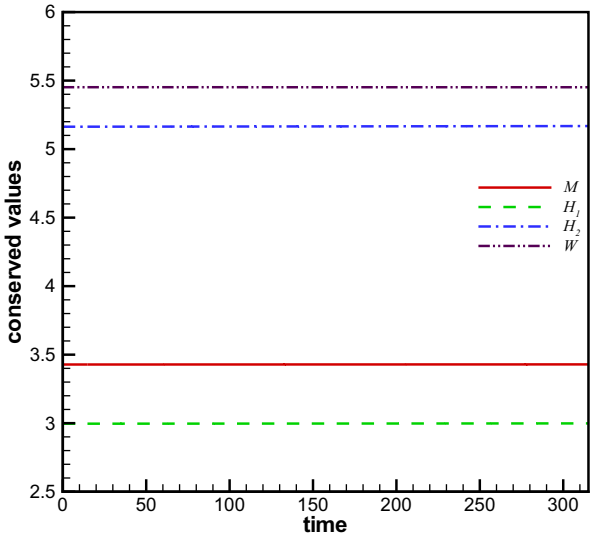

Fig. 6.2. Verification of the proposed algorithm. It shows that the quantities M, H_1, H_2, and W (see Eqs. (6.7) and (6.5)) for the travelling wave problem are well preserved by the proposed algorithm for $t > 300$ (the time period of 100 cycles, i.e. the initial waveform goes out and in the periodic domain 100 times.)

Table 6.1
The spatial rate of convergence for the problem considered in Fig. 6.1. Note that the time increment $\Delta t = 0.12308 \times 10^{-3}$ is much smaller than the grid size.

Number of cells N	32	64	128
Error in L_2 norm	5.8714E−03	1.686E−04	3.290E−06
Rate of convergence	–	5.121	5.679

Table 6.2
The temporal rate of convergence for the problem considered in Fig. 6.1. The number of cells in the calculation is $N = 128$.

Δt	2.46E−02	1.23E−02	6.15E−03
Error in L_2 norm	4.026E−03	1.025E−03	2.561E−04
Rate of convergence	–	1.973	2.000

convergence are shown in Tables 6.1 and 6.2, respectively. The convergence rates are found approximately 5.4 in space and 2 in time, respectively, for the proposed scheme.

Table 6.3 shows the comparison between the proposed method and the particle method developed in [8,9] at the final time $t = 3.1509$ (over one period). A fixed small time step $\Delta t = 0.12308 \times 10^{-3}$ is used for both methods. For such a small time step, the proposed method has much smaller errors compared with the particle method. Tables 6.4, 6.5 and 6.6 show similar comparisons of the two methods, but the solutions are computed using a fixed ratio of $c\frac{\Delta t}{\Delta x}$, where c is the wave speed. They show that the proposed method has smaller errors in the L_2 norm, but is less efficient than the particle method. They also show that when $c\frac{\Delta t}{\Delta x}$ decreases, the errors of the proposed method decrease as well, but there is no such effect for the particle method. It is no surprise that the overall rate of convergence is 2, when $c\frac{\Delta t}{\Delta x}$ is fixed, since a second-order time integrator is employed in the iterative algorithm. We are currently developing a sixth-order time integrator [12] for the proposed iterative algorithm. We remark that all calculations are performed on a laptop with Intel® Pentium® M 1.6 GHz, 768 MB DDR-RAM running on Microsoft® Windows® XP home edition.

6.2. Implicit midpoint time integrator

In this section, we demonstrate that the conserved quantities of the equation are well preserved by the implicit midpoint time integrator. Consider a non-periodic initial condition

$$u_0(x) = \operatorname{sech}(x) \tag{6.8}$$

Table 6.3
The spatial rate of convergence for the problem considered in Fig. 6.1. The time step used in the calculation is $\Delta t = 0.12308 \times 10^{-3}$.

Number of cells	Error in L_2 norm		Rate of convergence	
	Current method	Particle method	Current method	Particle method
$N = 32$	5.871E−03	1.339E−02	–	–
$N = 64$	1.686E−04	3.190E−03	5.121	2.069
$N = 128$	3.290E−06	7.532E−04	5.679	2.082
$N = 256$	1.268E−07	1.903E−04	4.697	1.984

Table 6.4
The errors and rate of convergence for the problem considered in Fig. 6.1. The time step used in the calculation is $c\frac{\Delta t}{\Delta x} = 1$, where c is the wave speed.

Number of cells	Error in L_2 norm		Rate of convergence		CPU time	
	Current method	Particle method	Current method	Particle method	Current method	Particle method
$N = 32$	4.999E−02	1.339E−02	–	–	1.40E−01	<1.0E−02
$N = 64$	1.497E−02	3.190E−03	1.739	2.069	7.65E−01	1.56E−02
$N = 28$	4.026E−03	7.532E−04	1.895	2.082	1.031	4.68E−02
$N = 256$	1.028E−03	1.903E−04	1.968	1.984	1.671	2.18E−01

Table 6.5
The errors and rate of convergence for the problem considered in Fig. 6.1. The time step used in the calculation satisfies $c\frac{\Delta t}{\Delta x} = \frac{1}{2}$.

Number of cells	Error in L_2 norm		Rate of convergence		CPU time	
	Current method	Particle method	Current method	Particle method	Current method	Particle method
$N = 32$	1.556E−02	1.339E−02	–	–	1.09E−01	<1.0E−02
$N = 64$	3.895E−03	3.190E−03	1.997	2.069	5.93E−01	3.12E−02
$N = 128$	1.025E−03	7.532E−04	1.926	2.082	8.59E−01	1.09E−01
$N = 256$	2.585E−04	1.903E−04	1.987	1.984	2.109	4.06E−01

Table 6.6
The errors and rate of convergence for the problem considered in Fig. 6.1. The time step used in the calculation satisfies $c\frac{\Delta t}{\Delta x} = \frac{1}{4}$.

Number of cells	Error in L_2 norm		Rate of convergence		CPU time	
	Current method	Particle method	Current method	Particle method	Current method	Particle method
$N = 32$	6.834E−03	1.339E−02	–	–	1.40E−01	1.56E−02
$N = 64$	9.083E−04	3.190E−03	2.911	2.069	7.50E−01	4.68E−02
$N = 128$	2.561E−04	7.532E−04	1.826	2.082	1.187	2.03E−01
$N = 256$	6.474E−05	1.903E−04	1.984	1.984	3.093	8.12E−01

embedded in the large periodic domain $L = 40$, as shown in Fig. 6.3(a). The periodic domain, $-20 \leqslant x \leqslant 20$, is uniformly divided into $N = 1280$ cells. Fig. 6.3(b)–(d) shows the numerical solutions with different values of κ at the final time $t = 10$ for the initial condition (6.8), demonstrating that the solution becomes more dispersive when κ increases, in the sense that more peaks occur when κ is large. Using this example, we compare three methods, the implicit midpoint integrator, the trapezoidal integrator (a symmetric time integrator), and the second-order BDF (BDF2) integrator for their capabilities of preserving the Hamiltonians. The simulations are run to the final time $t = 10$. The time step used for all three methods satisfies $\Delta t = \frac{1}{80}\Delta x$. The parameter κ is 100. With this magnitude of κ, there are more than a few peaks in the solution, and preservation of Hamiltonians becomes more difficult for a numerical algorithm. A good numerical algorithm should render well preserved Hamiltonians. Fig. 6.4(a) shows that the midpoint method and the trapezoidal method preserve the Hamiltonian H_1 very well compared with the BDF2 method. However, when we zoom in to the horizontal line in Fig. 6.4(a), we see in Fig. 6.4(b) that the trapezoidal method creates small fluctuations while the implicit midpoint produces little to no fluctuation.

6.3. Smooth travelling wave problem for $\kappa = 0$

In this example, we consider the non-dispersion case, $\kappa = 0$ in Eq. (1.1). Subjected to the initial conditions $\phi(0) = 1$ and $\phi_x(0) = 0$, the smooth travelling solution of the non-dispersive shallow-water wave equation in periodic domains has the form

$$u(x,t) = \phi(x - ct), \tag{6.9}$$

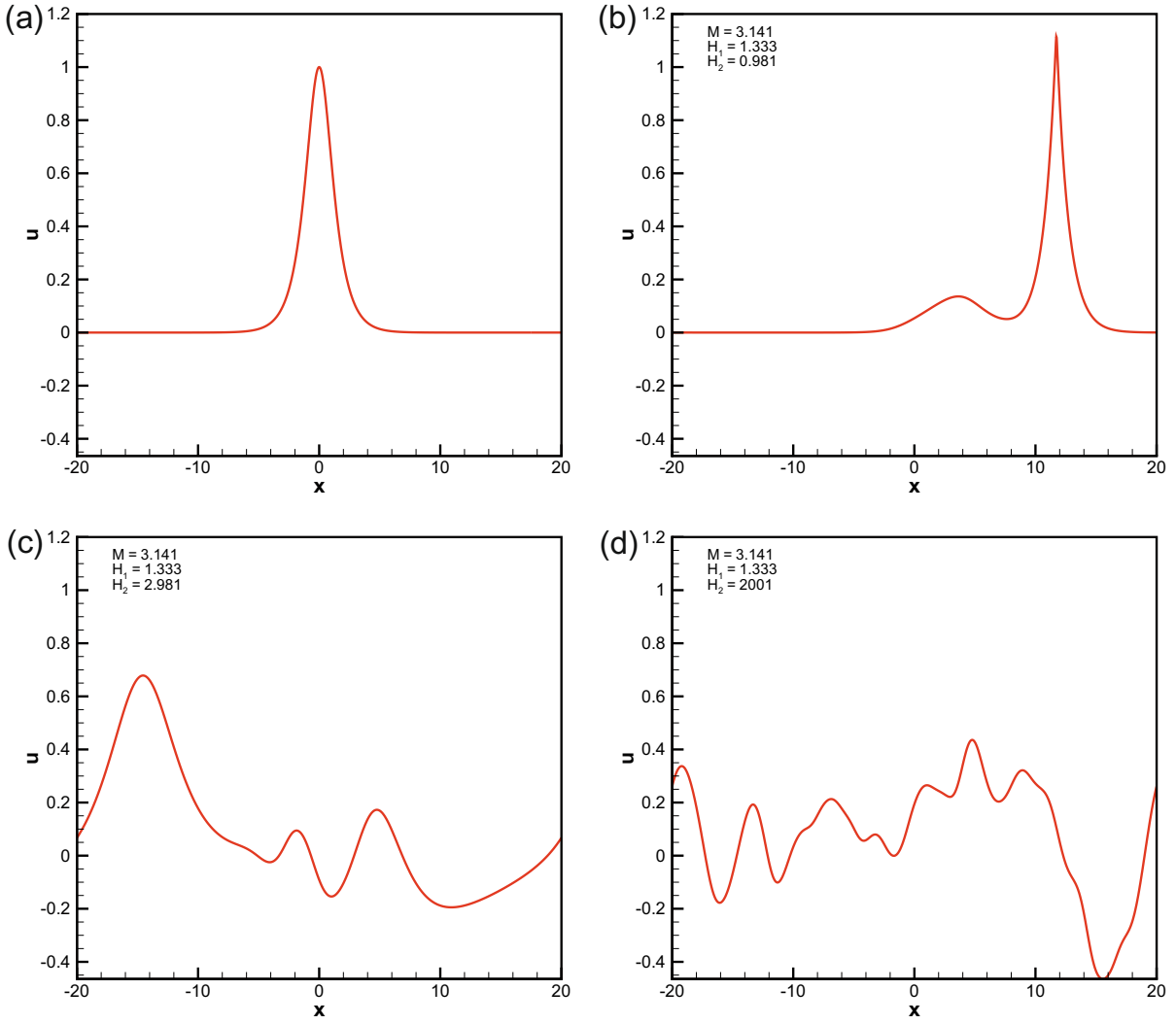

Fig. 6.3. The numerical solutions with different values of κ at the final time $t = 10$. The initial data embedded in a large periodic domain are non-periodic (6.8). The figures show that the solution becomes more dispersive when κ increases. (a) Initial condition; (b) $\kappa = 10^{-3}$; (c) $\kappa = 1$; (d) $\kappa = 10^{3}$.

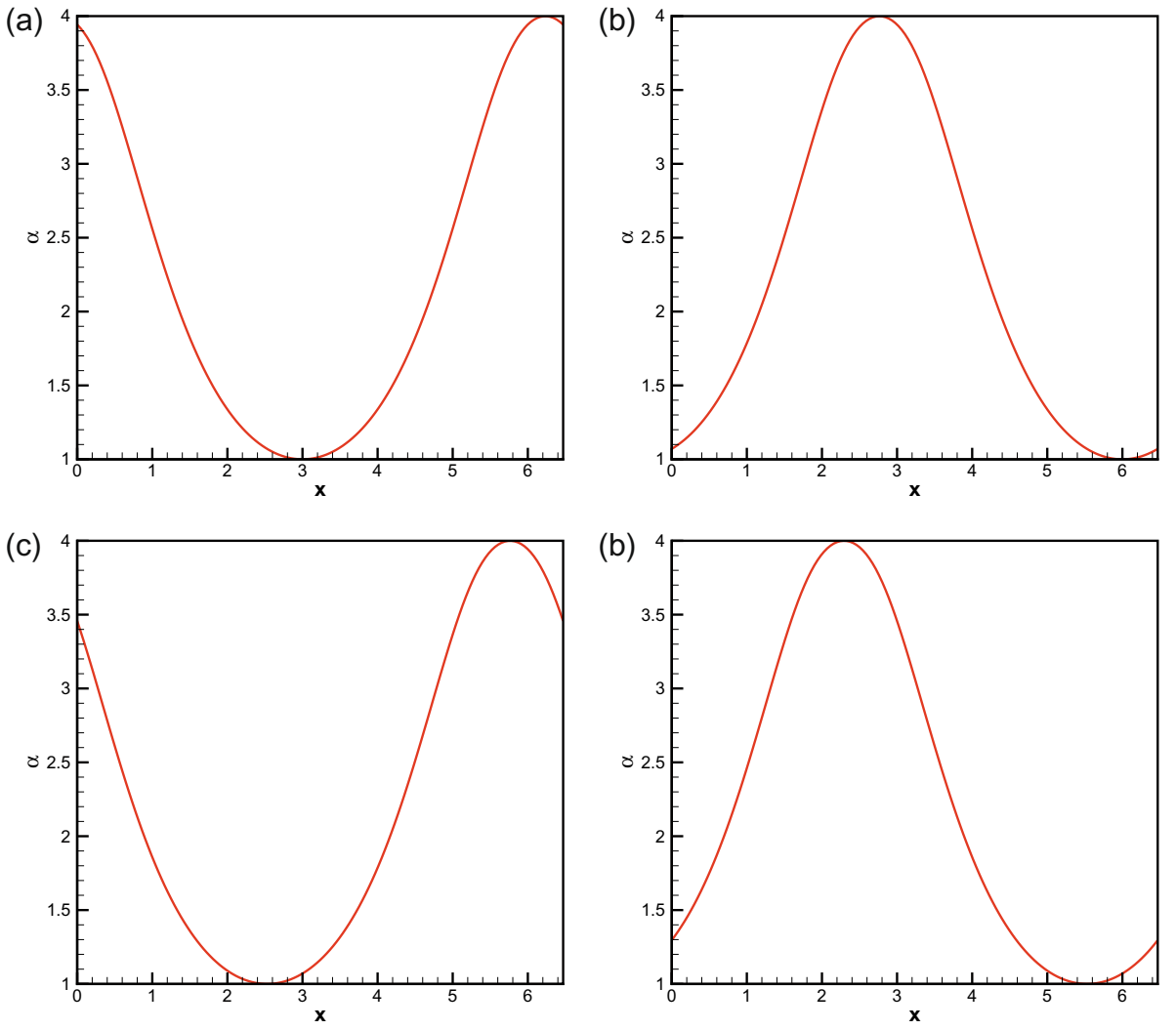

Fig. 6.5. Plots of energy density $\alpha = u^2 + u_x^2$ at different chosen times. (a) $t = 1$, (b) $t = 2$, (c) $t = 3$, and (d) $t = 4$. The plots show that α is a periodic function, which indicates the conservation of the Hamiltonian H_1 (see Eq. (6.7)).

the grid points used in our calculation are comparable to the numbers of the cells used in [24]. The numerical solution obtained with $N = 1{,}00{,}000$ is used as the reference solution [24]. The time step used in our calculation is $\Delta t = 10^{-4}$ for $N = 10,\ 20,\ 30$, and 60. The final time is $t = 0.5$. Table 6.7 shows that the errors of our algorithm are smaller than those reported in [24], in both L_2 and L_∞ norms.

6.4. Two-peakon solutions

In this example, we show that the proposed scheme has the ability to capture the peakon solutions. Consider the initial condition in a periodic domain

$$u_0(x) = \phi_1(x) + \phi_2(x), \tag{6.16}$$

where

$$\phi_i(x) = \left\{ \begin{array}{l} \frac{c_i}{\cosh(a/2)} \cosh(x - x_i); |x - x_i| \leqslant a/2 \\ \frac{c_i}{\cosh(a/2)} \cosh(a - (x - x_i)); |x - x_i| > a/2 \end{array} \right\}. \tag{6.17}$$

We choose the coefficients to be $c_1 = 2, c_2 = 1, x_1 = -5, x_2 = 5, a = 30$, which are the same as those employed in the paper by Xu and Shu [24]. Initially, the primary peakon is located at $x = 10$, and the secondary peakon is located at $x = 20$. The non-periodic initial condition is embedded in the periodic domain $0 \leqslant x \leqslant 30$. In Fig. 6.7, we present the grid refinement study for

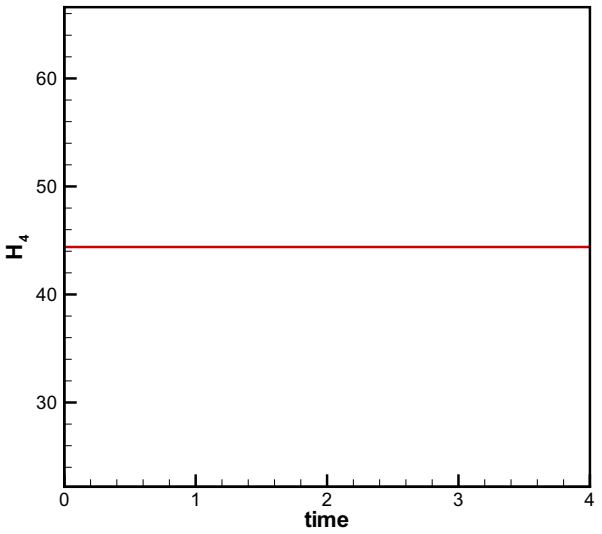

Fig. 6.6. The well preserved Hamiltonian H_4 (see Eq. (6.11)) by the proposed algorithm. The initial condition is a smooth travelling wave with $\kappa = 0$ in Eq. (1.1).

Table 6.7
The errors and spatial rates of convergence for the $\kappa = 0$, smooth travelling wave initial condition, (6.9) and (6.10) at $t = 0.5$. A periodic domain $0 \leqslant x \leqslant L \simeq 6.46954603635$ is used. The numerical solution obtained with $N = 1{,}00{,}000$ is used as the reference solution [24]. The time step used in the calculation is $\Delta t = 10^{-4}$ for $N = 10$, 20, 30, and 60. Note that the LDG method uses P2 elements with 10, 20, 40 and 80 cells.

Number of cells (number of element cells)	Error in L_2 norm		Rate of convergence		Error in L_∞ norm		Rate of convergence	
	Current method	P2-LDG method	Current method	P2-LDG method	Current method	P2-LDG method	Current method	P2-LDG method
$N = 10(10)$	2.704E−03	1.41E−03	–	–	6.061E−03	6.75E−03	–	–
$N = 20(20)$	8.472E−05	1.49E−04	4.996	3.24	2.110E−04	9.06E−04	4.843	2.90
$N = 30(40)$	1.579E−05	1.70E−05	4.142	3.13	4.851E−05	9.85E−05	3.626	3.20
$N = 60(80)$	1.512E−06	8.95E−06	3.384	2.88	3.039E−06	4.96E−05	3.996	3.07

the proposed algorithm using the two-peakon initial data. At the final time $t = 18$, both peakons travel out and in the periodic domain, and the primary peakon has overtaken the secondary peakon. Fig. 6.7(a) shows that visually our result has a good agreement with that reported in [24]. Their result was computed using the P5-LDG finite element method with 320 cells. In (b), we zoom in to the right-hand-side peak and notice that after refining the grid, so that when the number of cells is greater than $N = 3840$, our numerical solutions become visually grid-independent and are different from the result reported in [24]. Note that if the peak is located at one of the grid points, the second derivative u_{xx} at that point is assigned a large number initially, using the approximation of a one-sided second-order finite difference, and for the rest of grid points, the derivatives are found exactly.

6.5. Initial data with discontinuous derivatives

Consider the initial condition in the domain of $-30 \leqslant x \leqslant 30$,

$$u_0(x) = \frac{10}{(3 + |x|)^2}. \tag{6.18}$$

We perform the grid refinement study for this initial data. The solutions are computed with the number of cells $N = 640, N = 1280$, and $N = 1920$. Similar to the two-peakon initial data, if the discontinuity of derivative is located at one of the grid points, the second derivative u_{xx} at that point is assigned a large number initially, using the approximation of a one-sided second-order finite difference, and for the rest of grid points, the derivatives are found exactly. We compare the results with the LDG solutions in [24]. The LDG solutions use 320 uniform P2 elements in the same domain. Similar to the previous example, Fig. 6.8(a) shows that visually the two numerical solutions agree with each other quite well. If we zoom in to the primary peak, we notice that after refining the grid, so that when the number of grid point is greater than $N = 1280$, our solutions become visually grid-independent and are slightly different from the result reported in [24]. This example demonstrates that the proposed scheme is capable of resolving the emerging peak solutions.

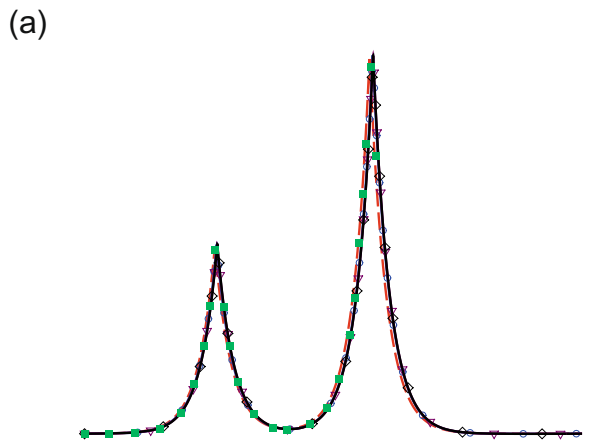

6.6. Soliton–antisoliton collision

For the limit case $\kappa = 0$, the two-soliton dynamics of the shallow-water wave equation are studied in detail in [3,4]. An exact solution is given for the perfectly antisymmetric "soliton-antisoliton" collision case. This is a numerically challenging problem, since the term uu_{xx} tends to a sum of delta functions when the collision occurs. This suggests that the right-hand-side of Eq. (1.3) becomes the derivative of a delta function when the collision occurs. To avoid this numerical difficulty, following the suggestion in [14], the Eq. (1.1) is written as an equivalent system of equations:

$$u_t + uu_x + P_x = 0, \tag{6.19}$$

$$-P_{xx} + P = \frac{1}{2}(u^2 + \alpha), \tag{6.20}$$

$$\alpha_t + (u\alpha)_x = (u^3 - 2Pu)_x, \tag{6.21}$$

where $\alpha = u^2 + u_x^2$. The two-step iterative method developed for solving Eqs. (1.3) and (1.2) alternately can be used to solve the above system of equations. In the first step, instead of solving one Eq. (1.3), we solve two Eqs. (6.19) and (6.21), to obtain the next iteration of u and α. In the second step, we solve a Helmholtz equation to obtain the next iteration of the auxiliary

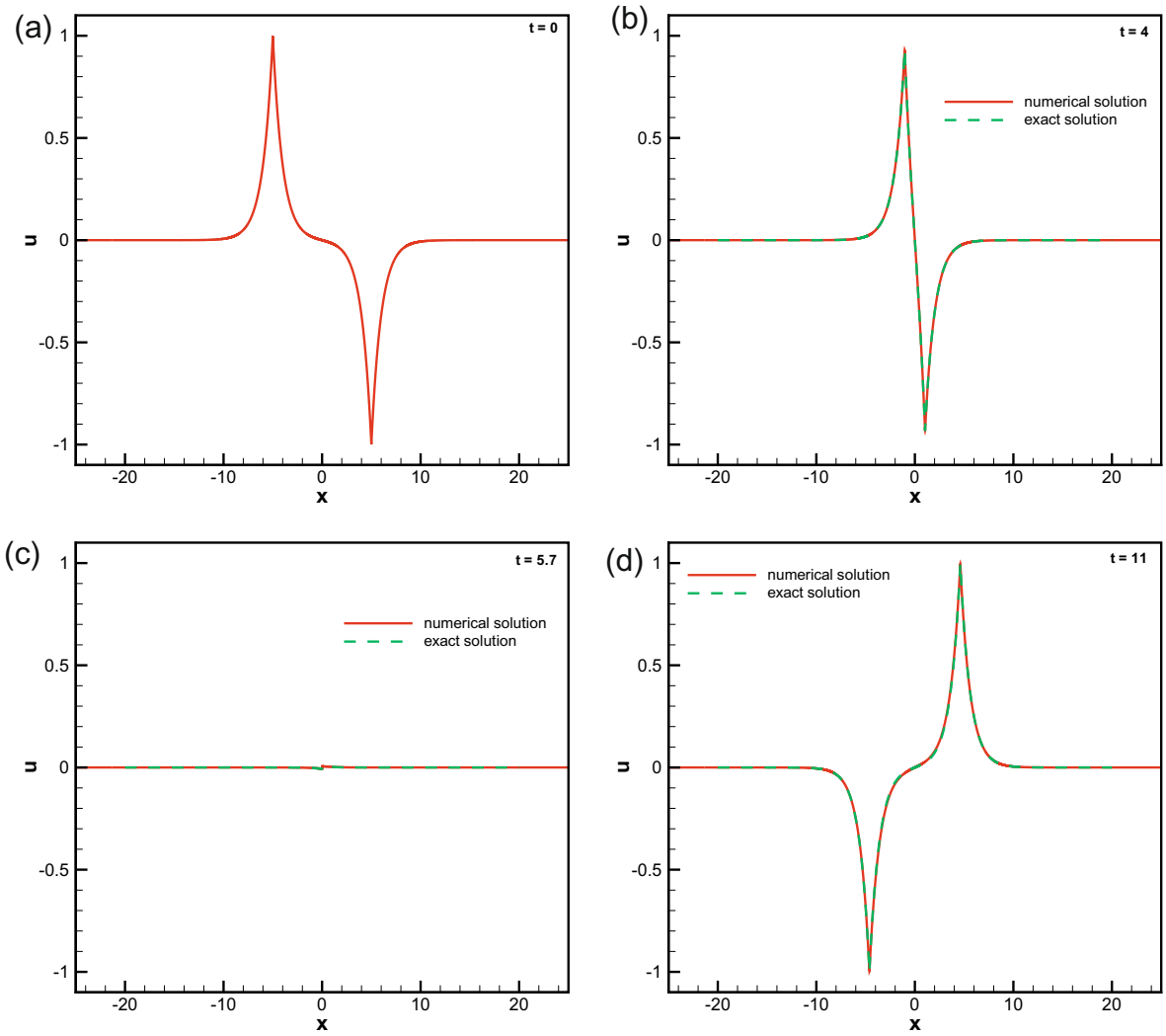

Fig. 6.9. The soliton–antisoltoin collision: (a) is the initial condition, (b) is the beginning of the collision, (c) is the approximate time of the collision, and (d) is post collision. The theoretical wave speed is $c \simeq 0.999977$, and the theoretical collision time is $t_c \simeq 5.69327$. The computed solutions are compared with the exact solutions in the figures. The simulation figures show that the proposed scheme not only accurately captures the wave speed and the collision time, but the numerical solutions are indistinguishable from the exact solutions.

variable P. The dispersion-relation-preserving scheme, the three-point compact Helmholtz solver, and the implicit midpoint time integrator all remain unchanged.

Consider the soliton–antisoliton initial condition

$$u_0(x) = e^{-|x+5|} - e^{-|x-5|}. \tag{6.22}$$

The collision time t_c and the wave speed c can be obtained by solving equation (4.26) in [4]

$$\begin{aligned} 10 &= -2\log[\operatorname{sech}(-ct_c)], \\ 2 &= \frac{-2c}{\tanh(-ct_c)}. \end{aligned} \tag{6.23}$$

Solving the above equations, we have $c \simeq 0.999977299777468$ and $t_c \simeq 5.693265068768256$. Following the notations in [4], we write solutions of the soliton–antisoliton collision as

$$u(x,t) = \frac{c}{\tanh(c(t-t_c))}[e^{-|x-q(t)|} - e^{-|x+q(t)|}], \tag{6.24}$$

where

$$q(t) = -\log[\operatorname{sech}^2(t-t_c)]. \tag{6.25}$$

Fig. 6.9(a)–(d) shows simulations of the soliton–antisoliton collision: (a) is the initial condition, (b) is the beginning of the collision, (c) is the approximate time of the collision, and (d) is post collision. The simulations compare solutions computed

[13] G.M. Coclite, K.H. Karlsen, N.H. Risebro, A convergent finite difference scheme for the Camassa–Holm equation with general H^1 initial data, SIAM J. Numer. Anal. 4 (2007) 771–795.
[14] D. Cohen, B. Owren, X. Raynaud, Multi-symplectic integration of the Camassa–Holm equation, J. Comput. Phys. 227 (2008) 5492–5512.
[15] J. De Frutos, J.M. Sanz-Serna, An easily implementable fourth-order method for the time integration of wave problems, J. Comput. Phys. 103 (1992) 160–168.
[16] H. Holden, X. Raynaud, A convergent numerical scheme for the Camassa–Holm equation based on multipeakons, DCDS-B 14 (2006) 503–523.
[17] H. Holden, X. Raynaud, Convergence of a finite difference scheme for the Camassa–Holm equation, SIAM J. Numer. Anal. 44 (2006) 1655–1680.
[18] R.S. Johnson, Camassa–Holm, Korteweg-de Vries and related models for water waves, JFM 455 (2002) 63–82.
[19] H. Kalisch, J. Lenells, Numerical study of traveling-wave solutions for the Camassa–Holm equation, Chaos Soliton. Fract. 25 (2005) 287–298.
[20] H. Kalisch, X. Raynaud, Convergence of a spectral projection of the Camassa–Holm equation, Numer. Meth. Part. Diff. Equ. 22 (2006) 1197–1215.
[21] J. Lenells, Conservation laws of the Camassa–Holm equation, J. Phys. A 38 (2005) 869–880.
[22] C.K.W. Tam, J.C. Webb, Dispersion-relation-preserving finite difference schemes for computational acoustics, J. Comput. Phys. 107 (1992) 262–281.
[23] J. von Neumann, R.D. Richtmyer, A method for the numerical calculation on hydrodynamic shock, J. Appl. Phys. 21 (1950) 232–237.
[24] Y. Xu, C.W. Shu, A local discontinuous Galerkin method for the Camassa–Holm equation, SIAM J. Numer. Anal. 46 (2008) 1998–2021.